INORGANIC CHEMISTRY FRONTIERS

CCS 中国化学会 CHINESE CHEMICAL SOCIETY

ROYAL SOCIETY OF CHEMISTRY

Gelation-induced controlled synthesis of TiO2 with tunable phase transition for efficient photocatalytic hydrogen evolution

Journal:	*Inorganic Chemistry Frontiers*
Manuscript ID	QI-RES-01-2024-000193.R1
Article Type:	Research Article
Date Submitted by the Author:	29-Feb-2024
Complete List of Authors:	Lei, Wenwei; Yanshan University School of Environmental and Chemical Engineering, Ying, Wang; Yanshan University School of Environmental and Chemical Engineering Hongji, Wang; Yanshan University School of Environmental and Chemical Engineering Suzuki, Norihiro; Tokyo Denki University School of Engineering Evening Division, Department of Natural Sciences Terashima, Chiaki; Tokyo University of Science, Research Institute for Science & Technology Fujishima, Akira; Tokyo University of Science

ARTICLE

Gelation-induced controlled synthesis of TiO_2 with tunable phase transition for efficient photocatalytic hydrogen evolution

Received 00th January 20xx,
Accepted 00th January 20xx

DOI: 10.1039/x0xx00000x

Wenwei Lei,[*a] Ying Wang,[a] Hongji Wang,[a] Norihiro Suzuki,[b] Chiaki Terashima[*c] and Akira Fujishima [c, d]

Methods for the precise tailoring of heterophase junctions and the micro/nanostructure of high-crystallinity TiO_2 are indispensable for the synthesis of TiO_2-based photocatalytic materials with high activity exposure, accessibility, and stability. However, current strategies suffer from an inability to control phase composition, a need for special equipment, and complexity of precursor composition. Here, a facile gelation-induced phase transition strategy is demonstrated to synthesize TiO_2 with precisely tunable anatase and rutile phases by controlling the coordination mode of Ti^{4+} during gelation. The synthesized chestnut-shell A_{76}/R_{24}-TiO_2 has a phase composition similar to that of commercial P25 as well as a highly crystalline anatase/rutile phase, an interfacial heterogeneous structure and abundant surface oxygen vacancies. The synergistic effect of the heterogeneous structure junction and surface oxygen vacancies contributes to the charge separation efficiency and photocatalytic activity, endowing it with excellent photocatalytic hydrogen production activity, with or without the addition of a co-catalyst. Overall, this approach provides new insights and inspiration to explore the precise regulation of the phase composition of materials.

Introduction

With the ever-increasing expansion of human society and the explosive growth of industry, the consumption of fossil fuels as a main energy source is rapidly increasing.[1,2] As a result, environmental pollution and a need for renewable energy resources have become two of the most important issues facing the world today.[3,4] Accordingly, the development of new environmentally friendly, safe, clean, and sustainable energy sources has become an extremely urgent challenge.[5-7] Semiconductor photocatalysis is considered a promising strategy by which we can simultaneously mitigate the energy crisis and environmental pollution.[8-11] Since the first discovery of photocatalytic water splitting in 1972, TiO_2 has become recognized as one of the most promising photocatalysts owing to its chemical stability, non-toxicity, abundance, and low cost.[12-14] Since then, researchers have developed various methods, such as hydrothermal,[15,16] sol-gel,[17,18] precipitation,[19-21] and chemical vapor deposition,[22-24] for the preparation of novel and efficient TiO_2 photocatalysts. Nevertheless, despite many important developments, commercial P25, which must be prepared using complex and dedicated equipment via steam-fed flame aerosol methodology, remains the industry standard. Therefore, the facile synthesis of TiO_2 that exhibits high photocatalytic activity remains a significant challenge.

TiO_2 in natural minerals comprises a variety of crystal structures, such as anatase, rutile, and brookite.[25,26] It has been demonstrated that anatase has very good photocatalytic properties.[27,28] However, the wide band gap of anatase limits its absorption of visible light in photocatalysis, and the rapid recombination of photogenerated electron-hole pairs reduce its photocatalytic efficiency. This has promoted research into the modification of photocatalyst materials based on TiO_2. The phase heterojunction formed by the coupling of anatase and rutile particles promotes the transfer of photoexcited electrons at the anatase-rutile interface, enhancing charge separation and thus photocatalytic performance.[29-31] It is well known that the excellent photocatalytic performance of commercial P25 originates from the partial heterojunction between its anatase and rutile phases. However, current strategies for the development of this material are limited by difficultly in controlling the phase components, the requirement of special equipment, and the complexity of preparing precursor components.[32-34] Accordingly, a methodology for precisely adjusting the anatase-rutile ratios and micro-/nano-structures of TiO_2 is required. This is critical for the synthesis of photocatalytic TiO_2 materials with high activity exposure, high accessibility, and stability.

Herein, for the first time, a gelation-induced phase transition strategy is demonstrated for the synthesis of TiO_2 with precisely tuneable anatase and rutile phases, which is achieved by controlling the gelation process. Titanium tetrachloride ($TiCl_4$) is used as a precursor, regulating the gelation and coordination mode of Ti^{4+} by forming coordination complexes with the hydroxyl groups on the polyvinyl alcohol (PVA) chains as cross-linking sites, thus achieving regulation of the TiO_2 phase state.

[a] Hebei Key Laboratory of Nano-biotechnology, School of Environmental and School of Environmental and Chemical Engineering, Yanshan University, Qinhuangdao 066004, Hebei, China.
[b] Department of Natural Sciences, School of Engineering, Tokyo Denki University, 5 Senjyu Asahi-cho, Adachi-ku, Tokyo 120-8551, Japan
[c] Research Center for Space System Innovation, Tokyo University of Science, 2641 Yamazaki, Noda, Chiba 278-8510, Japan
[d] Institute of Photochemistry and Photomaterials, University of Shanghai for Science and Technology, Shanghai 2000093, P.R. China

† Footnotes relating to the title and/or authors should appear here.
Electronic Supplementary Information (ESI) available: [details of any supplementary information available should be included here]. See DOI: 10.1039/x0xx00000x

The resultant A_x/R_y- TiO_2, which has an adjustable anatase and rutile phase ratio (A_x and R_y represent the percentages of anatase and rutile phases, respectively), can be prepared by varying the concentration of $TiCl_4$. Interestingly, TiO_2 with a chestnut-shell-like micro-/nano-structure and an anatase-to-rutile phase ratio of 76:24 (A_{76}/R_{24}-TiO_2), which is similar to that of commercial P25, can be easily synthesized. Furthermore, A_{76}/R_{24}-TiO_2 has a more highly crystalline anatase/rutile phase, an interfacial heterogeneous structure, and more abundant surface oxygen vacancies than commercial P25. Therefore, the chestnut-shell-like A_{76}/R_{24}-TiO_2 shows excellent photocatalytic performance with a hydrogen evolution rate of 0.563 mmol h^{-1} using Pt as co-catalyst and of 68.19 μmol h^{-1} without a co-catalyst (based on 30 mg catalyst).

Experimental

The synthesis of A_xR_y-TiO_2

First, PVA is dissolved in N-methylpyrrolidone (NMP) solution with the assistance of heating to 110 °C to form a homogeneous solution. After that, $TiCl_4$ solution with different content (1.8 mmol, 2.7 mmol, 3.6 mmol, 4.5 mmol, and 5.4 mmol) was added quickly to the formed homogeneous PVA-NMP solution. The reaction mixture system was maintained at 110 °C for 3 hours. After that the above mixture system was hydrothermally treated at 180 °C for 24 h to fix the coordination mode of titanium ions and thus form TiO_2 with different crystalline phases. Finally, the A_x/R_y-TiO_2 nanoparticles could be obtained after the removal of soft polymer PVA by calcination in air at 500 °C for 3 hours. The chestnut shell-like A_{76}/R_{24}-TiO_2 could be synthesized by added 3.6 mmol of $TiCl_4$.

Photocatalytic hydrogen production

The photocatalytic activity of the catalyst was assessed by the production of hydrogen in aqueous methanol (20 vol%) and aqueous solutions under a solar simulator AM1.5(XENONLAMP POWER SUPPLY, MODDEL YSS-100A) with 1wt% Pt as the co-catalyst and without any of co-catalysts. Photocatalysts loaded with Pt was obtained by photo-deposition method using H_2PtCl_6 solution. A typical test is as follows: 30 mg of catalyst were dispersed by sonication (20 min) into 50 mL of aqueous methanol (20 vol%). The mixture was then poured into a 300 mL photoreaction cell that was covered with a quartz window, and bubbled with N_2 gas for 20 min to remove oxygen. During the photocatalysis, the suspension was continuously stirred to ensure uniform irradiation. 1 mL of gas was sampled from the reaction cell every hour after the start of the reaction, and injected into a gas chromatograph that was equipped with a thermal conductivity detector (GC-2014, Shimadzu, Japan) to quantify the gas composition.

Results and discussion

Chestnut-shell-like A_x/R_y-TiO_2 was synthesized via a gelation-induced phase transition strategy (Fig. 1A). In this approach, the $TiCl_4$ acts as a precursor and cross-linking agent, modulating coordination by regulating the gelation of PVA, which, in turn, ultimately plays the role of regulating the TiO_2 phase. First, PVA is dissolved in N-methylpyrrolidone (NMP) with heating at 110 °C to form a homogeneous solution. Then, the $TiCl_4$ solution is rapidly added to this solution, leading to a gradual transition from the original solution state to a phase-separation state and finally to a homogeneous gel state. The subsequently formed gel was solvothermally treated at 180 °C for 24 h to stabilize the coordination mode of the titanium ions and thus form TiO_2 with different crystalline phases. Finally, A_x/R_y-TiO_2 nanoparticles were obtained after the removal of the soft polymer PVA by calcination in air.

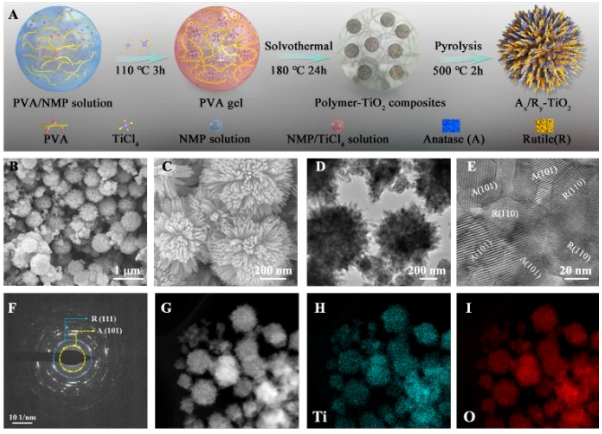

Fig.1 Synthesis and morphological/structural characteristics of A_xR_y-TiO_2. (A) Schematic of the synthesis of A_xR_y-TiO_2 by a facile self-assembly strategy of gelation-induced controlled phase transition. Low (B) and high (C) magnification SEM images; TEM (D) and HRTEM (E) images; and SAED patterns (F) of $A_{76}R_{24}$-TiO_2 prepared with 3.6 mmol $TiCl_4$, indicating the formation of anatase–rutile heterojunction TiO_2 nanoparticles. HAADF-STEM (G) and EDX elemental mapping images (H, I) of $A_{76}R_{24}$-TiO_2.

The scanning electron microscopy (SEM) image of A_{76}/R_{24}-TiO_2 shows a spherical configuration with a particle diameter of ~500 nm (Fig. 1B). The spheres are composed of many homogeneous nanorods forming a chestnut-shell-like surface morphology with a large surface area. The magnified SEM images (Fig. 1C) confirm that uniformly dispersed nanorods (~10 nm diameter) form nanospheres. The transmission electron microscopy (TEM) images (Fig. 1D) of A_{76}/R_{24}-TiO_2 confirm the presence of spherical nanoparticles composed of numerous nanorods. The high-resolution TEM (HRTEM) images (Fig. 1E) show highly crystalline (101) and (110) crystal planes representing the anatase and rutile phases of TiO_2, respectively, and these are interconnected to form a Z-scheme anatase and rutile heterostructure photocatalyst. As shown in Fig. 1F, the selected area electron diffraction (SAED) pattern shows two series of well-defined diffraction patterns attributed to polycrystalline anatase and rutile, respectively, further indicating the formation of anatase-rutile heterojunctions. In addition, the high-angle annular dark field scanning TEM (HAADF-STEM) images and corresponding EDS elemental mapping images demonstrate that Ti and O elements are homogeneously distributed within the nanospheres, as shown in Figs. 1G-I.

The gelation-induced phase-transition strategy can be used for the structural regulation of TiO_2, including adjustment of its anatase/rutile ratio and morphology, by changing the synthesis conditions. Fig. 2A shows a photograph of the PVA gelation process observed with the addition of different amounts of $TiCl_4$. Photograph Fig. 2A (a_0) shows the initial clear PVA-NMP solution, and (a-e) shows the solutions after adding 1.8, 2.7, 3.6, 4.5, and 5.4 mmol of $TiCl_4$, respectively. It can be seen that when a small amount of $TiCl_4$ is added, the polymer undergoes a desolvation process due to the strong ionization effect of $TiCl_4$. Thus, the hydrogen bonds between NMP and PVA are broken and PVA gradually starts to phase separate and precipitate out, as shown in Fig. 2A (a and b). When the amount of $TiCl_4$ is increased to 3.6 mmol, the excess $TiCl_4$ forms a coordination complex with the hydroxyl groups of PVA as a cross-linker, allowing the PVA to form a homogeneous gel (Fig. 2A-c). For the addition of $TiCl_4$ in amounts greater than 3.6 mmol, the PVA solutions all exhibit a well-gelled state (Fig. 2A (d and e)). Finally, ligand cross-linking was stabilized by the solvothermal method, after which TiO_2 is obtained in a controlled-phase-state by high-temperature calcination.

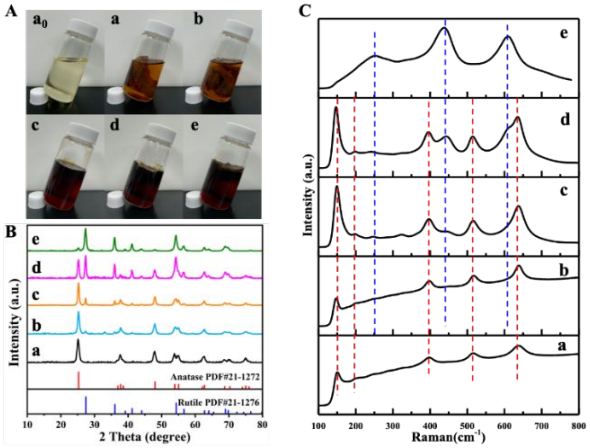

Fig. 2 Gelation-induced controlled TiO_2 phase regulation. (A) Optical photographs showing the gelation states of samples after the addition of different amount of $TiCl_4$. XRD patterns (B) and Raman spectra (C) of A_xR_y-TiO_2, indicating that the phase composition can be controllably adjusted by changing the concentration of $TiCl_4$. (a0) 0, (a) 1.8 mmol, (b) 2.7 mmol, (c) 3.6 mmol, (d) 4.5 mmol, (e) 5.4 mmol.

The crystal phases and compositions of the prepared TiO_2 were confirmed by wide-angle X-ray diffraction (WXRD) analysis. $TiCl_4$ can be directly used to regulate the synthesis of biphasic anatase/rutile TiO_2 (A_x/R_y), which can be verified from the anatase (JCPDS No. 21-1272) and rutile (JCPDS No. 21-1276) phase indexes, respectively. As shown in Fig. 2B, the characteristic diffraction peaks at 25.354°, 36.883°, 37.784°, 38.506°, 48.076°, 53.921°, 55.114°, and 62.726° of the anatase phase in the synthesized TiO_2, corresponding to the (101), (103), (004), (112), (200), (105), (211), and (213) crystal planes, gradually weaken with the amount of $TiCl_4$ added, while the characteristic diffraction peaks at 27.506°, 36.042°, and 41.186° of the rutile phase, corresponding to the (110), (101), and (111) crystal planes, gradually strengthen. When 1.8 mmol $TiCl_4$ is added, 100% anatase TiO_2 is obtained; however, when the addition amount is 3.6 mmol, the anatase-to-rutile ratio is 76:24, which is almost identical to the phase composition of commercial P25. When the addition amount is 5.4 mmol or more, almost-pure rutile-phase TiO_2 is produced. This demonstrates a gradual increase in the of rutile-to-anatase ratio from 0% to 100% with increasing $TiCl_4$ addition. The specific values can be calculated from the XRD pattern using Spurr and Myers' formula.[35] The phase components of A_xR_y-TiO_2 are summarized in Table 1.

Raman spectroscopy was used to analyse the crystalline phase composition of all the samples. As shown in Fig. 2C, the peaks at 151, 398, 515, and 638 cm^{-1} represent the vibrational modes of the anatase phase (marked with red dashed lines),[36] and the three peaks at 232, 442, and 609 cm^{-1} are assigned to the characteristic vibrations of the rutile phase (marked with blue dashed lines).[37] With increasing $TiCl_4$ addition, characteristic rutile-phase peaks emerge. Fig. 2C (b-d) clearly demonstrate the appearance of the rutile phase, as evidenced by the characteristic rutile Raman shifts at 230 and 449 cm^{-1}. Eventually, only the characteristic rutile Raman peaks can be seen (Fig. 2C-e), indicating that almost pure rutile TiO_2 can be obtained by this method of regulation. The above results are in full agreement with the XRD data, which prove that TiO_2 with different phase compositions can be controllably prepared by regulating the amount of $TiCl_4$. With changing TiO_2 phase composition, the morphological structure gradually changes from short spike-like clusters to spherical chestnut-shell-like structures, and finally to nanosheet structures (Fig. S1). N_2 adsorption-desorption experiments were performed to determine the pore volume, pore diameter, and surface area of all the samples, and the resultant data are summarized in Table 1.

The crystal structure of TiO_2 is known to constitute different arrangements of octahedra [TiO_6] and lattice distortions, which originate from the dehydration of octahedral charged complexes $[Ti(OH)_nCl_{6-n}]^{2-}$ formed by partial hydrolysis of Ti^{4+} with -OH and Cl^- in solution.[38-40] Thus, complex formation and dehydration are the key factors in determining the TiO_2 crystal structure. In this study, the formation of hydrogen bonds between NMP molecules and the hydroxyl groups on the PVA chains allowed them to form a homogeneous solution in the initial state, and when $TiCl_4$ was added, its strong ionization effect disrupted this hydrogen bonding, allowing the Ti^{4+} to gradually coordinate with the hydroxyl groups and form coordination complexes $[Ti(OH)_nCl_{6-n}]^{2-}$.

At low concentrations of $TiCl_4$(Fig. 3A), Ti^{4+} can form complexes with more -OH, which leads to a greater tendency to form edge-sharing octahedral complexes by a two-dehydration reaction, resulting in easier formation of anatase phases. In this state, the polymer undergoes a desolvation process and gradual phase separation in solution, leading to the precipitation of PVA chains. Conversely, at higher concentrations of $TiCl_4$ (Fig. 3B), the abundance of Cl^- results in fewer -OH groups being available for the formation of octahedral complexes. Therefore, the formation of corner-shared octahedral complexes through

dehydration leads to the formation of the rutile phase. Such abundant complex cross-linking sites allow the PVA gelation process to form a well-defined three-dimensional network structure. However, at low concentrations of $TiCl_4$, the abundance of -OH groups allow the octahedral coordination complexes to form symmetrical geometries, resulting in less lattice distortion and easy formation of the anatase phase. At high concentration, the coordination mode is diverse and the formation of octahedral complexes results in poor symmetry, which aggravates the lattice distortion and produces the rutile phase. This suggests that the process of gelation dictates the mode of formation and the distortion of octahedral ligands, which in turn regulates the crystalline phase structure of TiO_2.

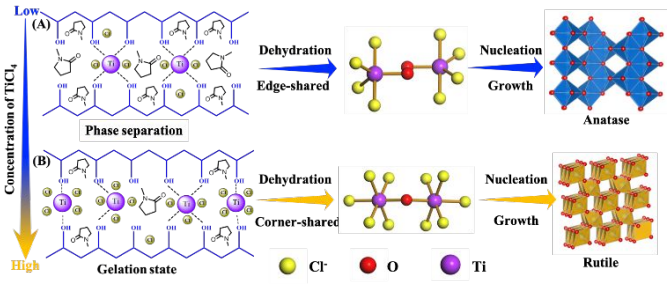

Fig. 3 Schematic diagram of the cross-linking mode and dehydration between $Ti(OH)_nCl_{6-n}]^{2-}$ complexes and the nucleation process of TiO_2.

Table 1. Structural and physical properties of photocatalysts prepared under different conditions.

Samples	$TiCl_4$ content (mmol)	Surface area[a] ($m^2\ g^{-1}$)	Pore volume[b] ($cm\ g^{-1}$)	Pore diameter (nm)	Composition[c]
a	1.8	29.98	0.13	2.43	Anatase
b	2.7	34.35	0.11	6.18	A: R = 92:8
c	3.6	45.77	0.21	13.82	A: R = 76:24
d	4.5	45.75	0.22	9.23	A: R = 44:56
e	5.4	35.95	0.13	4.74	A: R = 7:93
P25	--	43.2	0.24	2.43	A: R = 77:23

[a] BET specific surface areas calculated using nitrogen adsorption–desorption isotherms. [b] Pore volumes estimated based on the volume adsorbed at $P/P_0 = 0.99$. [c] Ratio of anatase(A)/rutile(R) estimated from XRD patterns.

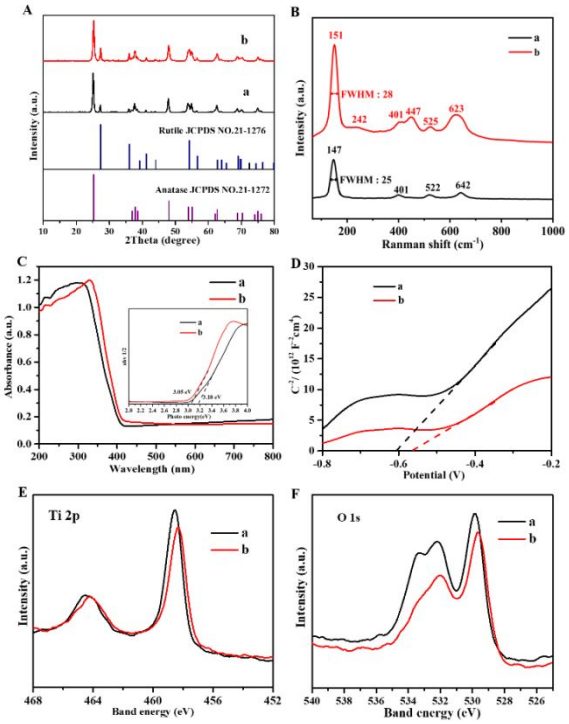

Fig. 4 Physicochemical properties of P25 (a) and synthesized chestnut-shell-like A_{76}/R_{24}-TiO_2 (b). (A) XRD patterns. (B) Raman spectra. (C) UV–Vis diffuse reflectance spectra. The inset in (C) is the corresponding Kubelka–Munk plot transformed from the UV–Vis diffuse reflectance spectra data. (D) Mott–Schottky plots. High-resolution Ti 2p (E) and O1s (F) XPS spectra. The black line (a) represents commercial P25 and the red line (b) represents A_{76}/R_{24}-TiO_2.

A comprehensive comparison of the physicochemical properties of the synthesized chestnut-shell-like A_{76}/R_{24}-TiO_2 and P25 is presented in Fig. 4. The XRD pattern of A_{76}/R_{24}-TiO_2 (Fig. 4A) shows two sets of diffraction peaks that can be assigned to the anatase (JCPDS No. 21-1272) and rutile (JCPDS No. 21-1276) phases. The anatase/rutile ratio was measured as ~76:24, which is similar to that of commercial P25 (~79:21). Fig. 4B shows the Raman spectrum of A_{76}/R_{24}-TiO_2, which clearly presents typical bands representing the anatase phase at 151, 401, 525, and 623 cm^{-1} and rutile phase at 242 and 447 cm^{-1}. Compared with those in the Raman spectrum of P25, the representative bands of the rutile phase in A_{76}/R_{24}-TiO_2 are more prominent, which indicates the more obvious heterogeneous structural composition of the anatase and rutile phases on the surface of the synthesized A_{76}/R_{24}-TiO_2. The peak of A_{76}/R_{24}-TiO_2 belonging to O-Ti-O is significantly shifted from 147 cm^{-1} to 151 cm^{-1} and the peak is broadened compared to P25. The full-width-half-maximum (FWHM) is calculated by Lorentz fitting and Gaussian fitting curves (Fig.4B). This indicates that the symmetry of the TiO_2 lattice is weakened due to surface lattice disorder or localized defects such as O-vacancies.[41] Typical type-IV curves with hysteresis loops and sharp capillary condensation steps at $P/P_0 = 0.5$-0.8 can be observed in the N_2 sorption isotherms for A_{76}/R_{24}-TiO_2 (Fig. S2). The Brunauer-Emmett-Teller (BET) surface area and pore volume are 45.77 $m^2\ g^{-1}$ and 0.21 $cm^3\ g^{-1}$, respectively. These results confirm the mesoporous structure of the material, which provides abundant active sites and facilitates the diffusion of

reactants and product ions/molecules, thus improving photocatalytic performance.

The UV-Vis absorption spectra of A_{76}/R_{24}-TiO_2 (Fig. 4C) exhibit a red-shift (compared with those of commercial P25) from 400-410 nm. The band gap of the A_{76}/R_{24}-TiO_2 is calculated to be ~3.05 eV by the Tauc function (inset in Fig. 4C), which is lower than that of for commercial P25 (3.18 eV). The Mott-Schottky curves in Fig. 4D show a positive slope, with a relatively lower slope for A_{76}/R_{24}- TiO_2 than that of commercial P25, indicating faster charge transfer and increased donor density.[35,42] The full X-ray photoelectron spectroscopy (XPS) spectra of A_{76}/R_{24}-TiO_2 and commercial P25 are similar (Fig. S3), indicating that they have similar chemical compositions and no impurities. Fig. 4E and 4F show the high-resolution XPS spectra for the Ti 2p and O 1s orbitals of the two photocatalysts. The bond energies of Ti for 2p and O 1s of A_{76}/R_{24}-TiO_2 are lower than those of commercial P25. These downshifts are due to the known band bending effect caused by additional electrons in the oxygen vacancies (Ov) on the TiO_2 lattice and the change in the Ti chemical state (Ti^{4+} species), which also agree well with the electron paramagnetic resonance (EPR) spectra results. The EPR spectra (Fig. S4) of A_{76}/R_{24}-TiO_2 exhibit a strong signal at g = 2.002, which is identified as the electron trap at O_v. The surface O_v plays a crucial role in narrowing the band gap to enhance light absorption and accelerate the transport of photogenerated electrons.

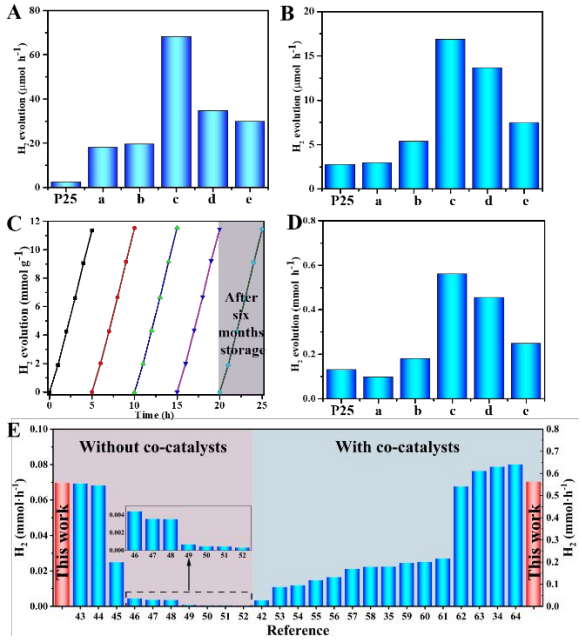

Fig. 5 Comparisons of photocatalytic H_2 generation rates for various TiO_2 photocatalysts under AM 1.5 light irradiation (A) and visible-light (λ >400 nm) (B) without addition of co-catalyst. (C) Recycling results for A_{76}/R_{24}-TiO_2 for H_2 evolution under AM 1.5 G illumination without addition of co-catalyst (hydrogen production by the photocatalyst after six months storage is also given). (D) Comparisons of photocatalytic H_2 generation rates for various TiO_2 photocatalysts under AM 1.5 light irradiation with 1wt% Pt as co-catalyst. (E) Comparison of the H_2 evolution efficiencies of TiO_2-based catalysts with and without co-catalysts (main comparison under the same light source conditions: AM 1.5 G, 100 mw cm^{-1}. Details in Table S1 and Table S2).

The photocatalytic properties of A_x/R_y-TiO_2 and commercial P25 were first evaluated by photocatalytic H_2 evolution under AM 1.5 light irradiation without addition of any co-catalyst. As shown in Fig. S5 all photocatalytic H_2 evolution curves are time-dependent, indicating a gradual increase in H_2 production. The chestnut-shell-like A_{76}/R_{24}-TiO_2 microspheres show a photocatalytic H_2 evolution rate of 68.19 μmol h^{-1} (Fig. 5A), which is much higher than those of commercial P25 (2.415 μmol h^{-1}), A_{100}- TiO_2 (18.09 μmol h^{-1}), A_{92}/R_8-TiO_2 (19.47 μmol h^{-1}), A_{44}/R_{56}- TiO_2 (34.71 μmol h^{-1}), and A_7/R_{93}-TiO_2 (29.82 μmol h^{-1}). The photocatalytic H_2 evolution performances (Fig. 5B) of all the samples were assessed under visible light by cutting off the UV light at wavelengths shorter than 400 nm. The H_2 generation rate of A_{76}/R_{24}-TiO_2 reaches 16.875 μmol h^{-1}, which is significantly higher than that of the other samples and six-fold higher than that of P25 (2.751 μmol h^{-1}). The photocatalytic degradation performance of A_{76}/R_{24}-TiO_2 and commercial P25 for methylene blue was also investigated without the use of a co-catalyst (Fig. S6). The photocatalytic decomposition of methylene blue (10 mg L^{-1}) over A_{76}/R_{24}-TiO_2 was completed within 60 min, whereas that over commercial P25 was completed in 80 min. In addition, chestnut-shell-like A_{76}/R_{24}-TiO_2 microspheres exhibit high stability as a photocatalyst. As shown in Fig. 5C, no significant decrease in photocatalytic hydrogen production was observed in the cycling test. Furthermore, the high H_2 production rate of 66 μmol h^{-1} was maintained after six months of storage at room temperature with less than 3% attenuation, confirming the high stability of the photocatalyst. XRD and XPS tests of A_{76}/R_{24}-TiO_2 before and after 6 cycles (24h) of photocatalytic hydrogen production showed that the curves were consistent before and after the reaction, which further proved the stability of its structure (Fig.S7). As shown in Fig. 5D, the H_2 generation rates of all the photocatalysts were evaluated with 1wt% Pt as a co-catalyst. Under these conditions, the H_2 generation rate of A_{76}/R_{24}-TiO_2 is nearly 0.563 mmol h^{-1}, which is 4.3-times that using commercial P25 (0.131 mmol h^{-1}). A_{76}/R_{24}-TiO_2 exhibits excellent photocatalytic H_2 production performance under AM 1.5 light irradiation, surpassing most hydrogen production rates reported for TiO_2 without co-catalysts,[43-52] and even some coloured TiO_2 catalysts. With the assistance of co-catalysts, the hydrogen production performance of A_{76}/R_{24}-TiO_2 is further improved and even higher than that of current efficient single-atom co-catalytic systems (Fig. 5E, Tables S1-2).[34,35,42,53-64]

To investigate the origin of this high photocatalytic performance without the addition of co-catalyst, a series of photoelectrochemical studies were conducted. Fig. S8 shows the results of photocurrent versus time tests. A_{76}/R_{24}-TiO_2 shows a higher photocurrent density, which may be due to Ov effectively facilitating the separation of electron-hole pairs. The electrochemical impedance spectroscopy (EIS) analysis results (Fig. S9) show that the impedance arc radius of A_{76}/R_{24}-TiO_2 is

much smaller than that of commercial P25, indicating that the uniform distribution of heterophase junctions in A_{76}/R_{24}-TiO_2 facilitates the transfer and separation of photogenerated charge carriers. Photoluminescence (PL) spectroscopy was used to further evaluate the charge-transfer and separation efficiency of the photocatalysts. A_{76}/R_{24}-TiO_2 shows a low PL intensity compared with commercial P25 (Fig. S10), indicating that charge recombination is better suppressed in A_{76}/R_{24}-TiO_2. Based on the above analysis, the excellent photocatalytic performance of A_{76}/R_{24}-TiO_2 is mainly due to (i) its chestnut-shell-like micro- and nanomorphology, which provides more exposed catalytically active sites for surface reduction reactions; (ii) the precisely controllable phase composition and the uniformly dispersed highly crystalline and heterogeneous anatase and rutile phase structure, which accelerates the separation and transport of charges at the phase interface; (iii) the presence of O_v, which act as active sites similar to noble-metal co-catalysts that can trap and transfer electrons for proton reduction, resulting in efficient hydrogen evolution.

Conclusions

In summary, we have successfully developed a facile gelation-assisted coordination self-assembly method for fabrication of TiO_2 photocatalysts with controlled phase structures and morphologies. $TiCl_4$ as a Ti source can be used to regulate the gelation of PVA solutions by forming coordination complexes with the hydroxyl groups on the PVA chains, allowing them to act as cross-linking sites. Thus, precise regulation of the phase composition (rutile: 0%-100%) can be achieved by regulating the amount of $TiCl_4$ added. The prepared A_{76}/R_{24}-TiO_2 has a chestnut-shell-like spherical shape and a highly crystalline anatase/rutile phase structure with a phase composition similar to that of commercial P25, as well as an abundance of surface oxygen vacancies. As a result of these excellent properties, A_{76}/R_{24}-TiO_2 shows excellent photocatalytic H_2 production rates of 68.19 μmol h^{-1} (without any noble-metal co-catalyst) and 0.563 mmol h^{-1} (using Pt as co-catalyst under AM 1.5 light irradiation), both of which are superior to those of P25. Our proposed strategy overcomes the problems associated with the conventional preparation methodology in terms of controlling the TiO_2 phase composition, the requirement of special equipment, raw materials and the complexity of preparing precursor components (a comprehensive comparison of several methods that can adjust the composition of the TiO_2 phase is presented in the table S3.), providing a promising research avenue for the design and fabrication of photocatalytic TiO_2 materials with controlled phase heterojunctions.

Author Contributions

This manuscript was written through the contributions of all authors. W. W. Lei: conceptualization, methodology, investigation, supervision, and writing – original draft. Y. Wang, H. J. Wang and N. Suzuki: data curation. review & editing. C. Terashima, W. W. Lei and A. Fujishima: resources, writing – review, supervision.

Conflicts of interest

There are no conflicts to declare.

Acknowledgements

The authors acknowledge financial support from the National Natural Science Foundation of Hebei province (No. B2021203028) and Hebei Province introduction of overseas students funding project (No. C20210327). Furthermore, this work was partially supported by the Japan Science and Technology Strategic International Collaborative Research Program (JSTSICORP) Grant JPMJSC18H1 and the Japan Science and Technology Program on Open Innovation Platform with Enterprises, Research Institute, and Academia (JST OPERA) Grant JPMJOP1843.

References

1. N. Bolson, P. Prieto and T. Patzek, Capacity factors for electrical power generation from renewable and nonrenewable sources, *Proc. Natl. Acad. Sci.*, 2022, **119**, e2205429119.
2. S. Motesharrei, J. Rivas, E. Kalnay, G. R. Asrar, A. J. Busalacchi, R. F. Cahalan, M. A. Cane, R. R. Colwell, K. Feng, R. S. Franklin, K. Hubacek, F. Miralles-Wilhelm, T. Miyoshi, M. Ruth, R. Sagdeev, A. Shirmohammadi, J. Shukla, J. Srebric, V. M. Yakovenko and N. Zeng, Modeling Sustainability: Population, Inequality, Consumption, and Bidirectional Coupling of the Earth and Human Systems, *Natl. Sci. Rev.*, 2016, **3**, 470-494.
3. M. Wang, S. Liu, T. Qian, J. Liu, J. Zhou, H. Ji, J. Xiong, J. Zhong and C. Yan, Over 56.55% Faradaic efficiency of ambient ammonia synthesis enabled by positively shifting the reaction potential, *Nat. Commun.*, 2019, **10**, 341.
4. H.-N. Wang, Y.-H. Zou, H.-X. Sun, Y. Chen, S.-L. Li and Y.-Q. Lan, Recent progress and perspectives in heterogeneous photocatalytic CO_2 reduction through a solid-gas mode, *Coord. Chem. Rev.*, 2021, **438**, 213906.
5. M. Liu, C. Wei, H. Zhuzhang, J. Zhou, Z. Pan, W. Lin, Z. Yu, G. Zhang and X. Wang, Fully Condensed Poly (Triazine Imide) Crystals: Extended π-Conjugation and Structural Defects for Overall Water Splitting, *Angew. Chem., Int. Ed.*, 2022, **61**, e202113389.
6. Y. Yan, J. Lin, K. Huang, X. Zheng, L. Qiao, S. Liu, J. Cao, S. C. Jun, Y. Yamauchi and J. Qi, Tensile Strain-Mediated Spinel Ferrites Enable Superior Oxygen Evolution Activity, *J. Am. Chem. Soc.*, 2023, **145**, 24218-24229.
7. Y. Yan, J. Lin, T. Xu, B. Liu, K. Huang, L. Qiao, S. Liu, J. Cao, S. C. Jun, Y. Yamauchi and J. Qi, Atomic-Level Platinum Filling into Ni-Vacancies of Dual-Deficient NiO for Boosting Electrocatalytic Hydrogen Evolution, *Adv. Energy Mater.*, 2022, **12**, 2200434.
8. L. Zhang, J. Zhang, H. Yu and J. Yu, Emerging S - Scheme Photocatalyst, *Adv. Mater.*, 2022, **34**, 2107668.
9. X. Li, F. Ye, H. Zhang, M. Ahmad, Z. Zeng, S. Wang, S. Wang, D. Gao and Q. Zhang, Ternary rGO decorated $W_{18}O_{49}$ @g-C_3N_4 composite as a full-spectrum-responded Z-scheme photocatalyst for efficient photocatalytic H_2O_2 production and water disinfection, *Journal of Environmental Chemical Engineering*, 2023, **11**, 110329.
10. M. Liras, M. Barawi and V. A. de la Peña O'Shea, Hybrid materials based on conjugated polymers and inorganic semiconductors as

photocatalysts: from environmental to energy applications, *Chem. Soc. Rev.*, 2019, **48**, 5454-5487.
11. Z. Xiao, C. Zhang, P. Li, D. Wang, X. Zhang, L. Wang, J.-j. Zou and G. Li, Engineering oxygen vacancies on Tb-doped ceria supported Pt catalyst for hydrogen production through steam reforming of long-chain hydrocarbon fuels, *Chin. J. Chem. Eng.*, 2024, DOI: https://doi.org/10.1016/j.cjche.2023.12.008.
12. A. Fujishima and K. Honda, Electrochemical Photolysis of Water at a Semiconductor Electrode, *Nature*, 1972, **238**, 37-38.
13. A. Meng, L. Zhang, B. Cheng and J. Yu, Dual Cocatalysts in TiO_2 Photocatalysis, *Adv. Mater.*, 2019, **31**, 1807660.
14. E. J. W. Crossland, N. Noel, V. Sivaram, T. Leijtens, J. A. Alexander-Webber and H. J. Snaith, Mesoporous TiO_2 single crystals delivering enhanced mobility and optoelectronic device performance, *Nature*, 2013, **495**, 215-219.
15. V. Kurnaravel, S. Mathew, J. Bartlett and S. C. Pillai, Photocatalytic hydrogen production using metal doped TiO_2: A review of recent advances, *Appl. Catal., B*, 2019, **244**, 1021-1064.
16. K. Mori, K. Maki, S. Kawasaki, S. Yuan and H. Yamashita, Hydrothermal synthesis of TiO_2 photocatalysts in the presence of NH_4F and their application for degradation of organic compounds, *Chem. Eng. Sci.*, 2008, **63**, 5066-5070.
17. J. Shen, M. Shi, B. Yan, H. Ma, N. Li and M. Ye, Ionic liquid-assisted one-step hydrothermal synthesis of TiO_2-reduced graphene oxide composites, *Nano Res.*, 2011, **4**, 795-806.
18. A. Giampiccolo, D. M. Tobaldi, S. G. Leonardi, B. J. Murdoch, M. P. Seabra, M. P. Ansell, G. Neri and R. J. Ball, Sol gel graphene/TiO_2 nanoparticles for the photocatalytic-assisted sensing and abatement of NO_2, *Appl. Catal., B*, 2019, **243**, 183-194.
19. R. Sharma, A. Sarkar, R. Jha, A. K. Sharma and D. Sharma, Sol-gel-mediated synthesis of TiO_2 nanocrystals: Structural, optical, and electrochemical properties, *Int. J. Appl. Ceram. Technol.*, 2020, **17**, 1400-1409.
20. Z. Wang, S. Liu, X. Cao, S. Wu, C. Liu, G. Li, W. Jiang, H. Wang, N. Wang and W. Ding, Preparation and characterization of TiO_2 nanoparticles by two different precipitation methods, *Ceram. Int.*, 2020, **46**, 15333-15341.
21. L. A. Calzada, C. Louis, C. W. Han, V. Ortalan and R. Zanella, Au-Ru/TiO_2 prepared by deposition-precipitation with urea: Relevant synthesis parameters to obtain bimetallic particles, *Appl. Catal., B*, 2020, **264**, 118503.
22. V. Serga, R. Burve, A. Krumina, M. Romanova, E. A. Kotomin and A. Popov, Extraction-Pyrolytic Method for TiO_2 Polymorphs Production, *Crystals*, 2021, **11**, 431.
23. A. Miquelot, L. Youssef, C. Villeneuve-Faure, N. Prud'homme, N. Dragoe, A. Nada, V. Rouessac, S. Roualdes, J. Bassil, M. Zakhour, M. Nakhl and C. Vahlas, In- and out-plane transport properties of chemical vapor deposited TiO_2 anatase films, *J. Mater. Sci.*, 2021, **56**, 10458-10476.
24. S. Jayawardena, H. D. Siriwardena, R. M. G. Rajapakse, A. Kubono and M. Shimomura, Fabrication of a quartz crystal microbalance sensor based on graphene oxide/TiO_2 composite for the detection of chemical vapors at room temperature, *Appl. Surf. Sci.*, 2019, **493**, 250-260.
25. S. E. Pratsinis, Flame aerosol synthesis of ceramic powders, *Progr. Energy Combust. Sci.*, 1998, **24**, 197-219.
26. A. Yamakata and J. J. M. Vequizo, Curious behaviors of photogenerated electrons and holes at the defects on anatase, rutile, and brookite TiO_2 powders: A review, *J. Photochem. Photobiol. C Photochem. Rev.*, 2019, **40**, 234-243.
27. J. Zhang, P. Zhou, J. Liu and J. Yu, New understanding of the difference of photocatalytic activity among anatase, rutile and brookite TiO_2, *Phys. Chem. Chem. Phys.*, 2014, **16**, 20382-20386.
28. T. Luttrell, S. Halpegamage, J. Tao, A. Kramer, E. Sutter and M. Batzill, Why is anatase a better photocatalyst than rutile? - Model studies on epitaxial TiO_2 films, *Sci. Rep.*, 2014, **4**, 4043.
29. Q. Wu, Z. Wu, Y. Li, H. Gao, L. Piao, T. Zhang and L. Du, Controllable Synthesis and Photocatalytic Activity of Anatase TiO_2 Single Crystals with Exposed {110} Facets, *Chin. J. Catal.*, 2012, **33**, 1743-1753.
30. T. Kawahara, Y. Konishi, H. Tada, N. Tohge, J. Nishii and S. Ito, A Patterned TiO_2 (Anatase)/TiO_2 (Rutile) Bilayer - Type Photocatalyst: Effect of the Anatase/Rutile Junction on the Photocatalytic Activity, *Angew. Chem., Int. Ed.*, 2002, **41**, 2811-2813.
31. J. Low, J. Yu, M. Jaroniec, S. Wageh and A. A. Al-Ghamdi, Heterojunction Photocatalysts, *Adv. Mater.*, 2017, **29**, 1601694.
32. J. Zhang, Q. Xu, Z. Feng, M. Li and C. Li, Importance of the relationship between surface phases and photocatalytic activity of TiO_2, *Angew. Chem., Int. Ed.*, 2008, **47**, 1766-1769.
33. R. Koirala, S. E. Pratsinis and A. Baiker, Synthesis of catalytic materials in flames: opportunities and challenges, *Chem. Soc. Rev.*, 2016, **45**, 3053-3068.
34. W. Zhang, H. He, Y. Tian, K. Lan, Q. Liu, C. Wang, Y. Liu, A. Elzatahry, R. Che, W. Li and D. Zhao, Synthesis of uniform ordered mesoporous TiO_2 microspheres with controllable phase junctions for efficient solar water splitting, *Chem. Sci.*, 2019, **10**, 1664-1670.
35. H. Xiong, L. Wu, Y. Liu, T. Gao, K. Li, Y. Long, R. Zhang, L. Zhang, Z.-A. Qiao, Q. Huo, X. Ge, S. Song and H. Zhang, Controllable Synthesis of Mesoporous TiO_2 Polymorphs with Tunable Crystal Structure for Enhanced Photocatalytic H_2 Production, *Adv. Energy Mater.*, 2019, **9**, 1901634.
36. R. A. Spurr and H. Myers, Quantitative Analysis of Anatase-Rutile Mixtures with an X-Ray Diffractometer, *Anal. Chem.*, 1957, **29**, 760-762.
37. T. Ohsaka, F. Izumi and Y. Fujiki, Raman spectrum of anatase, TiO_2, *J. Raman Spectrosc.*, 1978, **7**, 321-324.
38. Y. Hara and M. Nicol, Raman spectra and the structure of rutile at high pressures, *Phys. Status Solidi B*, 1979, **94**, 317-322.
39. J.-G. Li, T. Ishigaki and X. Sun, Anatase, brookite, and rutile nanocrystals via redox reactions under mild hydrothermal conditions: Phase-selective synthesis and physicochemical properties, *J. Phys. Chem. C*, 2007, **111**, 4969-4976.
40. H. Cheng, J. Ma, Z. Zhao and L. Qi, Hydrothermal Preparation of Uniform Nanosize Rutile and Anatase Particles, *Chem. Mater.*, 1995, **7**, 663-671.
41. X. Bi, G. Du, A. Kalam, D. Sun, Y. Yu, Q. Su, B. Xu and A. G. Al-Sehemi, Tuning oxygen vacancy content in TiO2 nanoparticles to enhance the photocatalytic performance, *Chem. Eng. Sci.*, 2021, **234**, 116440.
42. C. Yang, Z. Wang, T. Lin, H. Yin, X. Lü, D. Wan, T. Xu, C. Zheng, J. Lin, F. Huang, X. Xie and M. Jiang, Core-Shell Nanostructured "Black" Rutile Titania as Excellent Catalyst for Hydrogen Production Enhanced by Sulfur Doping, *J. Am. Chem. Soc.*, 2013, **135**, 17831-17838.
43. Y. Jiang, H. Ning, C. Tian, B. Jiang, Q. Li, H. Yan, X. Zhang, J. Wang, L. Jing and H. Fu, Single-crystal TiO_2 nanorods assembly for efficient and stable cocatalyst-free photocatalytic hydrogen evolution, *Appl. Catal., B*, 2018, **229**, 1-7.
44. K. Zhang, L. Wang, J. K. Kim, M. Ma, G. Veerappan, C.-L. Lee, K.-j. Kong, H. Lee and J. H. Park, An order/disorder/water junction system for highly efficient co-catalyst-free photocatalytic hydrogen generation, *Energy Environ. Sci.*, 2016, **9**, 499-503.
45. D. Ding, Z. Jiang, D. Ji, M. Nosang Vincent and L. Zan, Bi_2O_2Se as a

novel co-catalyst for photocatalytic hydrogen evolution reaction, *Chem. Eng. J.*, 2020, **400**, 125931.

46. L. Sun, Y. Yuan, F. Wang, Y. Zhao, W. Zhan and X. Han, Selective wet-chemical etching to create TiO_2@MOF frame heterostructure for efficient photocatalytic hydrogen evolution, *Nano Energy*, 2020, **74**, 104909.
47. N. L. Reddy, D. P. Kumar and M. V. Shankar, Co-catalyst free Titanate Nanorods for improved Hydrogen production under solar light irradiation, *J. Chem. Sci. (Bangalore, India)*, 2016, **128**, 649-656.
48. T.-D. Nguyen-Phan, S. Luo, Z. Liu, A. D. Gamalski, J. Tao, W. Xu, E. A. Stach, D. E. Polyansky, S. D. Senanayake, E. Fujita and J. A. Rodriguez, Striving Toward Noble-Metal-Free Photocatalytic Water Splitting: The Hydrogenated-Graphene-TiO_2 Prototype, *Chem. Mater.*, 2015, **27**, 6282-6296.
49. G. Jia, Y. Wang, X. Cui and W. Zheng, Highly Carbon-Doped TiO_2 Derived from MXene Boosting the Photocatalytic Hydrogen Evolution, *ACS Sustainable Chem. Eng.*, 2018, **6**, 13480-13486.
50. N. Liu, X. Zhou, N. T. Nguyen, K. Peters, F. Zoller, I. Hwang, C. Schneider, M. E. Miehlich, D. Freitag, K. Meyer, D. Fattakhova-Rohlfing and P. Schmuki, Black Magic in Gray Titania: Noble-Metal-Free Photocatalytic H_2 Evolution from Hydrogenated Anatase, *ChemSusChem*, 2017, **10**, 62-67.
51. N. Liu, C. Schneider, D. Freitag, U. Venkatesan, V. R. R. Marthala, M. Hartmann, B. Winter, E. Spiecker, A. Osvet, E. M. Zolnhofer, K. Meyer, T. Nakajima, X. Zhou and P. Schmuki, Hydrogenated Anatase: Strong Photocatalytic Dihydrogen Evolution without the Use of a Co-Catalyst, *Angew. Chem., Int. Ed.*, 2014, **53**, 14201-14205.
52. X. Zhou, N. Liu, J. Schmidt, A. Kahnt, A. Osvet, S. Romeis, E. M. Zolnhofer, V. R. R. Marthala, D. M. Guldi, W. Peukert, M. Hartmann, K. Meyer and P. Schmuki, Noble-Metal-Free Photocatalytic Hydrogen Evolution Activity: The Impact of Ball Milling Anatase Nanopowders with TiH_2, *Adv. Mater.*, 2017, **29**, 1604747.
53. J. Liu, J. Ke, Y. Li, B. Liu, L. Wang, H. Xiao and S. Wang, Co_3O_4 quantum dots/TiO_2 nanobelt hybrids for highly efficient photocatalytic overall water splitting, *Appl. Catal., B*, 2018, **236**, 396-403.
54. M. Xiao, L. Zhang, B. Luo, M. Lyu, Z. Wang, H. Huang, S. Wang, A. Du and L. Wang, Molten‐Salt‐Mediated Synthesis of an Atomic Nickel Co‐catalyst on TiO_2 for Improved Photocatalytic H_2 Evolution, *Angew. Chem., Int. Ed.*, 2020, **59**, 7230-7234.
55. J. Xi, X. Zhang, X. Zhou, X. Wu, S. Wang, W. Yu, N. Yan, K. P. Loh and Q.-H. Xu, Titanium dioxide hierarchical microspheres decorated with atomically dispersed platinum as an efficient photocatalyst for hydrogen evolution, *J. Colloid Interface Sci.*, 2022, **623**, 799-807.
56. C. Wang, X. Kang, J. Liu, D. Wang, N. Wang, J. Chen, J. Wang, C. Tian and H. Fu, Ultrathin black TiO_2 nanosheet-assembled microspheres with high stability for efficient solar-driven photocatalytic hydrogen evolution, *Inorg. Chem. Front.*, 2023, **10**, 1153-1163.
57. X. Wu, S. Zuo, M. Qiu, Y. Li, Y. Zhang, P. An, J. Zhang, H. Zhang and J. Zhang, Atomically defined Co on two-dimensional TiO_2 nanosheet for photocatalytic hydrogen evolution, *Chem. Eng. J.*, 2021, **420**, 127681.
58. Y. Ma, Y. Zhang, Y. Ma, T. Lv, B. Xiao, X. Kuang, X. Deng, J. Zhang, J. Zhao and Q. Liu, *In situ* Cu single atoms anchoring on MOF-derived porous TiO_2 for the efficient separation of photon-generated carriers and photocatalytic H_2 evolution, *Nanoscale*, 2022, **14**, 15889-15896.
59. L. Li, J. Yan, T. Wang, Z.-J. Zhao, J. Zhang, J. Gong and N. Guan, Sub-10 nm rutile titanium dioxide nanoparticles for efficient visible-light-driven photocatalytic hydrogen production, *Nat. Commun.*, 2015, **6**, 5881.
60. X. Chen, L. Liu, P. Y. Yu and S. S. Mao, Increasing Solar Absorption for Photocatalysis with Black Hydrogenated Titanium Dioxide Nanocrystals, *Science*, 2011, **331**, 746-750.
61. Z. Zheng, B. Huang, J. Lu, Z. Wang, X. Qin, X. Zhang, Y. Dai and M.-H. Whangbo, Hydrogenated titania: synergy of surface modification and morphology improvement for enhanced photocatalytic activity, *Chem. Commun. (Cambridge, U. K.)*, 2012, **48**, 5733.
62. S. Hu, P. Qiao, L. Zhang, B. Jiang, Y. Gao, F. Hou, B. Wu, Q. Li, Y. Jiang, C. Tian, W. Zhou, G. Tian and H. Fu, Assembly of TiO_2 ultrathin nanosheets with surface lattice distortion for solar-light-driven photocatalytic hydrogen evolution, *Appl. Catal., B*, 2018, **239**, 317-323.
63. K. Lan, R. Wang, W. Zhang, Z. Zhao, A. Elzatahry, X. Zhang, Y. Liu, D. Al-Dhayan, Y. Xia and D. Zhao, Mesoporous TiO_2 Microspheres with Precisely Controlled Crystallites and Architectures, *Chem*, 2018, **4**, 2436-2450.
64. Z. Wang, C. Yang, T. Lin, H. Yin, P. Chen, D. Wan, F. Xu, F. Huang, J. Lin, X. Xie and M. Jiang, Visible-light photocatalytic, solar thermal and photoelectrochemical properties of aluminium-reduced black titania, *Energy Environ. Sci.*, 2013, **6**, 3007.